


Nonlinear behavior of electrohydrodynamic flow in viscoelastic fluidsZheng-Gang Su,^{1,2} Tian-Fu Li,³ Kang Luo,^{1,2} and Hong-Liang Yi ^{1,2,*}¹*School of Energy Science and Engineering, Harbin Institute of Technology, Harbin 150001, People's Republic of China*²*Key Laboratory of Aerospace Thermophysics, Ministry of Industry and Information Technology, Harbin 150001, People's Republic of China*³*Ji Hua Laboratory, Foshan 510006, Guangdong, People's Republic of China*

(Received 27 March 2021; accepted 20 August 2021; published 7 September 2021)

This paper presents a numerical study of electrohydrodynamic flow for the problem of electroconvection in a viscoelastic dielectric liquid subjected to unipolar injection. The nonlinear evolution of flow for diverse characteristic Weissenberg numbers is examined in detail. The influences of elasticity on the flow pattern, oscillation amplitude, current transfer, and power-law spectral scaling accompanying oscillatory flow are also investigated. The results demonstrate that the effect of viscoelasticity leads to hydrodynamic behaviors that are absent in Newtonian fluids. The transition sequences to the chaos of electroconvection in viscoelastic fluids are quite different from those in Newtonian fluids, and the elasticity precipitates the onset of chaos. An asymmetric steady flow pattern resulting from elasticity is observed in a perfectly symmetric geometry. The fluctuation amplitude of fluid motion is found to be suppressed for weakly elastic fluids but amplified when the fluid elasticity exceeds a certain threshold. For viscoelastic fluids, electric current transfer is reduced in most cases, but for weakly elastic fluid, it may be enhanced.

DOI: [10.1103/PhysRevFluids.6.093701](https://doi.org/10.1103/PhysRevFluids.6.093701)**I. INTRODUCTION**

Electrohydrodynamics (EHD) [1,2] describes the unique flow phenomena generated by the interaction between charged fluids and an applied electric field, which involves several disciplines, including fluid mechanics, electrochemistry, and electrodynamics. Fluid-driving technology based on EHD does not require traditional mechanical moving parts and permits the advantages such as lightweight structure, simple design, and low energy consumption. In an EHD system, the convective fluid can be a conductive liquid (an electrolyte solution of an acid, alkali, or salt) or a dielectric liquid such as silicone oil or ethanol. EHD flows involving the former liquids include electro-osmosis [3], which is characterized by a small scale, with the electric force acting mainly on the electric double layer near the electrode surface, and has received extensive attention in both academic research and engineering application. EHD phenomena involving dielectric liquids are also the basis of numerous engineering applications, such as electrostatic precipitation [4], electrospinning [5], EHD turbulent mixing [6], and techniques for enhancing heat [7,8] or mass [9] transfer. In contrast to the EHD flow of conductive liquids, the EHD flow mechanism in dielectric liquids is relatively complex, and the understanding of various related processes is still superficial.

Electroconvection [10,11] is an important subtopic within EHD. The electroconvection in dielectric liquids subjected to unipolar injection is a paradigmatic case of Coulomb-driven convection and is as fundamental a phenomenon in such liquids as Rayleigh-Bénard convection (RBC) is

*yihongliang@hit.edu.cn

in nonisothermal fluid [12]. When metal electrodes are placed in a dielectric liquid with low conductivity, electrochemical reactions may occur at the electrode-liquid interface under an electric field, and charge will be injected into the liquid. Under the action of the Coulomb force, the charge moves directionally and drives macroscopic flow. It is worth noting that dissociation of impurities is another way to generate ions in a dielectric liquid. However, a large number of experiments have shown that the ion injection is dominant compared with the dissociation process [13,14]. The flow in electroconvection is the result of complex and nonlinear interactions between charge transport, electric fields, and fluid motion. Experimental observation by Lacroix *et al.* [15] showed that the flow structure in electroconvection has a hexagonal pattern similar to that in RBC. Experiments [16,17] have also been conducted to evaluate the impact of the flow caused by the charge injection on heat transfer, and the results showed that heat transfer is increased significantly (up to an order of magnitude). For electroconvection between two plates with the charge injected homogeneously and autonomously, the flow exhibits linear instability corresponding to the onset of fluid motion. A series of stability analyses on electroconvection have been conducted by Atten and Lacroix [18], Schneider and Watson [19], Zhang and colleagues [20,21], and others. The study by Atten and Lacroix [18] confirmed the presence of a subcritical bifurcation in electroconvection characterized by a typical hysteresis loop [22].

Numerical simulation is another approach to gain detailed exploration of this problem. At first, the finite-difference method was adopted to solve the entire set of equations, but the false diffusion introduced by the numerical method made the result deviate greatly from the theoretical prediction. Subsequently, the particle-in-cell (PIC) method [23], the finite-element method combined with the PIC method [24] or the flux-corrected transport method [24], and the discontinuous Galerkin finite-element method [25] have been applied to numerical studies of electroconvection. Traoré *et al.* [12] combined the finite-volume method (FVM) with the total variation diminishing (TVD) scheme to solve the charge transport equation that is hyperbolic in nature. Luo *et al.* developed a unified lattice Boltzmann model [26] to simulate Coulomb-driven flows and obtained a hexagonal flow pattern [27] for the first time.

After the onset of convection, as the voltage increases further, the flow will evolve from a steady flow to oscillatory convection and will finally enter a chaotic state after several stages of periodic or quasiperiodic oscillations. The nonlinear process of electroconvection has a more prominent effect on the flow motion and heat transfer characteristics than steady electroconvection. RBC in a fluid layer heated from below is a well-known phenomenon, and the sequence of transitions from steady laminar to chaotic flow has been widely studied as a fundamental aspect of nonlinear hydrodynamics [28,29]. However, unlike the chaotic flow in RBC, that in electroconvection remains relatively unexplored [30,31]. Malraison and Atten [32] found two types of power spectra behavior of the electric current fluctuations in the viscous-dominated regime and the inertia-dominated regime. Castellanos *et al.* [33] investigated the maximum Lyapunov exponent of chaotic electroconvection for different instability parameters. Li *et al.* [34] identified three diverse transition routes to chaos in electrothermal convection.

According to their rheological characteristics, fluids can be divided into two basic types: Newtonian fluids and non-Newtonian fluids. The investigations of electroconvection mentioned above were generally carried out for simple Newtonian fluids, and with little attention being paid to the electroconvection in non-Newtonian fluids. Viscoelastic fluids [35,36] are a kind of non-Newtonian fluid with both viscosity and elasticity and exhibit complex mechanical behaviors such as elastic turbulence [37] and turbulent drag reduction [38]. To date, the nonlinear behavior of viscoelastic flow has been extensively studied theoretically, numerically, and experimentally [39]. The nonlinear process of electroconvection in a viscoelastic dielectric fluid will be affected by both inertial nonlinearity and elastic nonlinearity, which will lead to intriguing physical interactions in the flow. To the best of our knowledge, except for our previous study of the influence of elasticity on the onset of electroconvection [40], no research on the electroconvection of viscoelastic fluids subjected to unipolar injection has been reported. In our previous work, we focused on the types of bifurcation that occur in a fluid flow as the fluid loses its instability from a hydrostatic state to

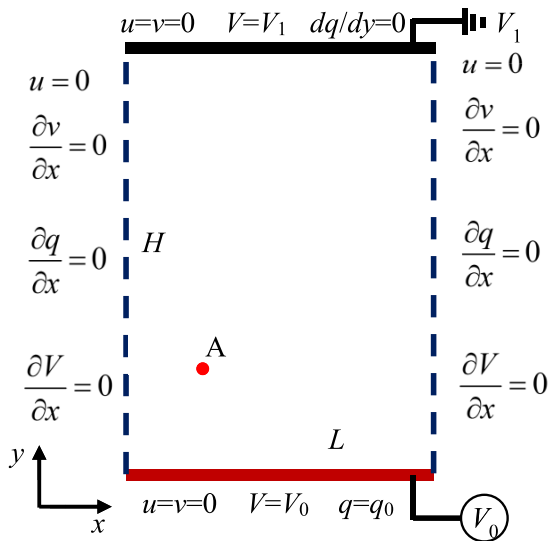


FIG. 1. Schematic illustration of the EHD system.

a convective state. Three different types of bifurcations have been found: subcritical bifurcation, supercritical bifurcation, and Hopf bifurcation. However, the transitions from stable to periodic and then to chaotic behavior as the driving parameters increase after the onset of convection have not been studied. In practical applications, unsteady convection and even turbulence are more common, and many types of nonlinear behaviors need to be investigated. The influence of elasticity on the unsteady flow behavior in electroconvection and the onset of chaos remains unexplored, and the associated laws of evolutionary and mechanisms of induction are yet to be studied. The effect of viscoelasticity of a fluid on heat transfer in thermal convection has also attracted much attention [41,42]. By contrast, there has been a lack of studies of the effect of viscoelasticity on the current transfer of EHD flows. Besides its fundamental academic interest, this topic is important for technological applications such as enhancement of mixing or heat transfer.

In this paper, we are interested in the dynamical evolution of unsteady electroconvection in viscoelastic fluids. We aim to investigate the effects of elasticity on flow patterns, oscillation amplitude, and electric current transfer accompanying nonlinear oscillatory behavior, and we then elucidate the physical mechanisms involved. The remainder of the paper is organized as follows. The physical problem and the relevant nondimensional governing equations and parameters are stated in Sec. II A. A brief introduction to the numerical method used in this paper is given in Sec. III. Then, in Sec. IV, the codes are verified, and the results of our computations are discussed. Finally, the conclusions are presented in Sec. V.

II. PROBLEM FORMULATION

The physical model of electroconvection in this paper is shown in Fig. 1. The dielectric liquid is confined between two parallel electrodes of length L and with a distance of H between them. The aspect ratio is defined as $A = L/H$. The potential difference $V_0 - V_1$ between the lower and upper electrode plates remains constant, and the left and right walls are assumed to be insulated. As far as the unipolar injection mechanism is concerned, the charge is assumed to be injected into the dielectric liquid from the lower emitter homogeneously and autonomously. The homogeneous and reproducible ion injection process can be achieved by covering the electrodes with ion-exchange membranes [43]. Under the action of the electric field, the fluid will lose its stability and be put into motion. This motion is assumed in this paper to be two dimensional, with the characters of

self-similar rolls [23]. To monitor and track the time-varying information of the flow field, point A with coordinates $(0.25L, 0.25H)$ at the lower-left corner of the cavity is selected as the sampling point.

The governing equations of electroconvection are the Navier-Stokes equations and a reduced set of Maxwell's equations in the electroquasistatic limit. In this paper, the fluid is assumed to be incompressible and with constant physical properties. The typical residual conductivity of the dielectric liquid is less than $10^{-11}\Omega^{-1}\text{ m}^{-1}$, and so it is reasonable to completely ignore the effects of magnetism and Joule heating [18]. The basic electrohydrodynamic equations can then be expressed as [11,22]

$$\nabla \cdot \mathbf{u} = 0, \quad (1)$$

$$\frac{\partial(\rho_0\mathbf{u})}{\partial t} + \nabla \cdot (\rho_0\mathbf{u}\mathbf{u}) = -\nabla p + \nabla \cdot \boldsymbol{\tau} + q\mathbf{E}, \quad (2)$$

$$\nabla^2 V = -q/\varepsilon, \quad (3)$$

$$\mathbf{E} = -\nabla V, \quad (4)$$

$$\frac{\partial q}{\partial t} + \nabla \cdot (qK\mathbf{E} - D\nabla q + q\mathbf{u}) = 0, \quad (5)$$

where ρ_0 is the density, ε is the permittivity, K is the ionic mobility, and D is the charge diffusion coefficient. In addition, $\mathbf{u} = [u, v]$ is the fluid velocity vector, $\mathbf{E} = [E_x, E_y]$ is the electric field vector, and $\boldsymbol{\tau}$ is the extra stress tensor. The characters p , V , and q represent fluid pressure, electric potential, and charge density, respectively.

The stress tensor $\boldsymbol{\tau}$ can be decomposed into two contributions from the solvent and polymer, respectively:

$$\boldsymbol{\tau} = \boldsymbol{\tau}_s + \boldsymbol{\tau}_p. \quad (6)$$

For the solvent contribution, the Newtonian law holds, and so

$$\boldsymbol{\tau}_s = \eta_s[\nabla\mathbf{u} + (\nabla\mathbf{u})^T], \quad (7)$$

where η_s is the solvent viscosity.

To describe the dynamics of the viscoelastic fluid, we adopt the well-known Oldroyd-B model, for which the constitutive equation is [44]

$$\boldsymbol{\tau}_p + \lambda \boldsymbol{\tau}_p^\nabla = \eta_p[\nabla\mathbf{u} + (\nabla\mathbf{u})^T], \quad (8)$$

where η_p is the viscosity of the viscoelastic solution, and λ is the relaxation time. $\boldsymbol{\tau}_p^\nabla$ represents the upper-convected time derivative [44]

$$\boldsymbol{\tau}_p^\nabla = \frac{\partial\boldsymbol{\tau}_p}{\partial t} + \nabla \cdot (\mathbf{u}\boldsymbol{\tau}_p) - \nabla(\mathbf{u})^T \cdot \boldsymbol{\tau}_p - \boldsymbol{\tau}_p \cdot \nabla\mathbf{u}. \quad (9)$$

To facilitate the numerical solution, we rewrite the Oldroyd-B constitutive equation in terms of the conformation tensor \mathbf{C} , and then

$$\boldsymbol{\tau}_p = \frac{\eta_p}{\lambda}(\mathbf{C} - \mathbf{I}), \quad (10)$$

where \mathbf{I} is the identity matrix. The general transport equation for the conformation tensor \mathbf{C} is

$$\frac{\partial\mathbf{C}}{\partial t} + \mathbf{u} \cdot \nabla\mathbf{C} = \mathbf{C} \cdot \nabla\mathbf{u} + \mathbf{C} \cdot \nabla\mathbf{u}^T - \frac{\mathbf{C} - \mathbf{I}}{\lambda}. \quad (11)$$

The physical variables can be nondimensionalized by introducing the following scalings:

$$(x^*, y^*) = \frac{(x, y)}{H}, \quad t^* = \frac{t}{H/u_0}, \quad \mathbf{u}^* = \frac{\mathbf{u}}{u_0}, \quad q^* = \frac{q}{q_0}, \quad V^* = \frac{V}{(V_0 - V_1)},$$

$$\mathbf{E}^* = \frac{\mathbf{E}}{(V_0 - V_1)/H}, \quad p^* = \frac{p}{\rho_0 u_0^2}. \quad (12)$$

The governing equations are now written in dimensionless form as [11,40]

$$\nabla \cdot \mathbf{u} = 0, \quad (13)$$

$$\frac{\partial \mathbf{u}}{\partial t} + \mathbf{u} \cdot \nabla \mathbf{u} = -\nabla p + \frac{\beta}{T/M^2} \nabla^2 \mathbf{u} + \frac{1-\beta}{Wi \cdot T/M^2} \nabla \cdot \mathbf{C} + CM^2 q \mathbf{E}, \quad (14)$$

$$\nabla^2 V = -Cq, \quad (15)$$

$$\mathbf{E} = -\nabla \phi, \quad (16)$$

$$\frac{\partial q}{\partial t} + \nabla \cdot (q(\mathbf{u} + \mathbf{E}) - \alpha \nabla q) = 0, \quad (17)$$

$$\frac{\partial \mathbf{C}}{\partial t} + \mathbf{u} \cdot \nabla \mathbf{C} = \mathbf{C} \cdot \nabla \mathbf{u} + \mathbf{C} \cdot \nabla \mathbf{u}^T - \frac{1}{Wi} \cdot [\mathbf{C} - \mathbf{I}]. \quad (18)$$

Six dimensionless parameters relevant to this problem appear in the above equations:

$$T = \frac{\varepsilon(V_0 - V_1)}{\eta K}, \quad C = \frac{q_0 H^2}{\varepsilon(V_0 - V_1)}, \quad M = \frac{1}{K} \left(\frac{\varepsilon}{\rho} \right)^{1/2},$$

$$\alpha = \frac{D}{K(V_0 - V_1)}, \quad Wi = \frac{\lambda u_0}{H}, \quad \beta = \frac{\eta_s}{\eta} = \frac{\eta_s}{\eta_s + \eta_p}. \quad (19)$$

Here, the electric Rayleigh number T is the ratio of the destabilizing Coulomb force to the stabilizing viscous force. C represents the charge injection strength. M is the ratio of the so-called hydrodynamic mobility of the ionic mobility to the actual ionic mobility, which represents the natures of the fluid and ion. M is greater than 3 for most situations [43]. α is the nondimensional charge diffusion number and is typically in the range of 10^{-4} to 10^{-3} [45]. Pérez and Castellanos [45] pointed out that the parameter $C/\alpha^{1/2}$ provides a measure of the relative importance of both mechanisms in the sense that diffusion becomes dominant for small values of $C/\alpha^{1/2}$ but is negligible in the limit $C/\alpha^{1/2} \rightarrow \infty$. In this paper, we choose the strong injection regimes ($C = 10$). Charge is mainly transported by fluid flow and the drift mechanism driven by the electric field, and the contribution of charge diffusion is extremely small compared with the migration term due to the electric field. Therefore, as in Refs. [8,11,46,47], the influence of charge diffusion is ignored in this paper. Wi is the Weissenberg number representing the ratio of the relaxation time of the viscoelastic fluid to the timescale of the flow. The retardation ratio β is the ratio of the solvent viscosity to the total viscosity η . In this paper, the typical values $C = 10$, $M = 10$, and $\beta = 0.8$ which are widely adopted in the literature, are held fixed unless otherwise specified.

In the EHD experiments by Malraison and Atten [32], it was found that each convective cell's basic oscillatory mechanism plays a vital effect in the form that the chaotic motion takes, and no difference with aspect ratio A has been found. Castellanos *et al.* [33] also agreed that the dynamics inside each cell essentially determine the chaotic fluid motion. The half wavelength of the most unstable model is equal to 0.614 for strong injection ($C = 10$) [48], and in our previous study [40], we found that the value does not change in a viscoelastic fluid when Wi does not exceed 0.5. Therefore, aiming to keep consistent with earlier studies [11,47] of the transition route to the chaos of electroconvection, we fix the aspect ratio $A = 0.614$ and apply symmetrical boundary conditions

at the lateral boundaries. For the initial condition, a rest state with zero field for all variables is used in our calculation. For the boundary conditions, the conformation tensor components are linearly extrapolated to the rigid walls and are applied with the zero-gradient condition at the symmetrical boundary. The other nondimensional boundary conditions are as follows:

at the bottom emitter: $u = v = 0$, $V = 1$, and $q = 1$;

at the top collector: $u = v = 0$, $V = 0$, and $dq/dy = 0$;

at the lateral boundaries: $u = 0$, $dV/dx = 0$, $dq/dx = 0$, $v = 0$ (free walls).

III. NUMERICAL METHODS

The FVM is exploited to discretize the differential equations presented in the previous section. To avoid pressure-velocity and stress-velocity decoupling, a staggered grid system with the velocity located at the cell faces and the other variables cell centered is adopted. As the fluid is assumed to be incompressible, the coupled equations are solved with the SIMPLER (semi-implicit method for pressure-linked equations revised) algorithm. For the time integration of all variables, a second-order semi-implicit three-time levels scheme is adopted. The central differencing scheme is used to discretize the diffusive term in the Navier-Stokes equations.

The conformation transport equation and the charge transport equation neglecting the diffusion term are typical hyperbolic equations, and so special attention must be paid. To prevent spurious numerical oscillations and preserve sharp gradients and a bounded solution, the TVD scheme [49] is recommended for discretization of the convective term of the charge transport equation. For a control volume, the charge across the cell interface k is evaluated as

$$q_k = q_C + \frac{1}{2}(q_D - q_C)\psi(r_k), \quad (20)$$

where $r_k = (q_C - q_U)/(q_D - q_C)$ is the smoothness indicator. The subscripts C , U , and D represent the central, upwind, and downwind control volumes related to interface k . The SMART scheme [50] for which the flux limiter $\psi(r_k) = \max(0, \min(2r_k, 0.75r_k + 0.25, 4))$ is adopted.

$$F_k = \dot{m}q_C + \frac{\dot{m}}{2}(q_D - q_C)\psi(r_k). \quad (21)$$

When Wi increases to a certain value, the growth of the conformation tensor becomes exponential. Directly solving the conformation transport equation will then increase the error and easily lead to numerical instabilities, in what is called the high Weissenberg number problem (HWNP) [51]. At present, one of the most effective methods to solve HWNP is the log-conformation representation developed by Fattal and Kupferman [52,53]. This representation cannot only maintain the symmetry and positive definiteness of the conformation tensor, but also reduce the calculation error at high Wi . The solution procedure is as follows.

Assuming that \mathbf{u} is a divergence-free velocity field and \mathbf{C} is a symmetric positive-definite tensor field, the velocity gradient $\nabla\mathbf{u}$ can be decomposed as follows:

$$\nabla\mathbf{u} = \boldsymbol{\Omega} + \mathbf{B} + \mathbf{N}\mathbf{C}^{-1}, \quad (22)$$

where $\boldsymbol{\Omega}$ is a pure rotational antisymmetric tensor, \mathbf{B} is a pure extension symmetric tensor, and \mathbf{N} is a pure rotational tensor (the antisymmetric tensor of the conformation tensor). Substitution of Eq. (22) into Eq. (18) then gives

$$\frac{\partial\mathbf{C}}{\partial t} + \mathbf{u} \cdot \nabla\mathbf{C} - (\boldsymbol{\Omega} \cdot \mathbf{C} - \mathbf{C} \cdot \boldsymbol{\Omega}) - 2\mathbf{B} \cdot \mathbf{C} = \frac{1}{Wi} \cdot [\mathbf{I} - \mathbf{C}]. \quad (23)$$

As the conformation tensor \mathbf{C} is symmetric and positive definite, it can be decomposed as follows:

$$\mathbf{C} = \mathbf{D}\mathbf{A}\mathbf{D}^T, \quad (24)$$

TABLE I. The maximum vertical velocity and the electric Nusselt number for various values of M for $T = 190$.

M	3	5	10	20	50	100
V_{\max} (Present)	3.149	3.515	3.745	3.810	3.819	3.820
V_{\max} (Wu <i>et al.</i>)	3.146	3.520	3.755	3.807	3.822	3.823
Ne (Present)	1.494	1.499	1.536	1.545	1.550	1.551
Ne (Wu <i>et al.</i>)	1.492	1.497	1.535	1.548	1.552	1.552

where \mathbf{D} is the matrix composed of the eigenvectors of \mathbf{C} , and $\mathbf{\Lambda}$ is the diagonal matrix composed of the eigenvalues of \mathbf{C} . The logarithmic form of \mathbf{C} is $\boldsymbol{\psi} = \log \mathbf{C} = \mathbf{D} \log(\mathbf{\Lambda}) \mathbf{D}^T$. Equation (23) can then be transformed into

$$\frac{\partial \boldsymbol{\psi}}{\partial t} + \mathbf{u} \cdot \nabla \boldsymbol{\psi} - (\boldsymbol{\Omega} \cdot \boldsymbol{\psi} - \boldsymbol{\psi} \cdot \boldsymbol{\Omega}) - 2\mathbf{B} = \mathbf{D} \cdot \frac{[\mathbf{\Lambda}^{-1} - \mathbf{I}]}{Wi} \cdot \mathbf{D}^T. \quad (25)$$

Finally, the task of solving the conformation transport equation is transformed into the task of solving Eq. (25). It can be seen that the product $\mathbf{B} \cdot \mathbf{C}$ reflecting the growth of \mathbf{C} in Eq. (18) is converted into the algebraic sum form of \mathbf{B} in Eq. (25), which effectively reduces the numerical error. Simultaneously, the above process can ensure the positive definiteness and symmetry of \mathbf{C} and enhance computational stability. Owing to its improved convergence properties, the Convergent and Universally Bounded Interpolation Scheme for the Treatment of Advection (CUBISTA) [54] is always adopted in the study of viscoelastic flows, and is adopted here to discretize the convective terms in Eq. (25) and the Navier-Stokes equations.

IV. RESULTS AND DISCUSSION

The time series of the maximum velocity V_{\max} is utilized to analyze the bifurcation of the solution. Similar to the Nusselt number in thermal convection, the electric Nusselt number N_e that represents the electric current intensity in electroconvection will also be output. N_e is defined as [11,55]

$$N_e = \frac{I_e}{I_0},$$

where I_0 denotes the conductive current when there is no fluid motion, and $I_e = \int_{y=\text{constant}} \frac{1}{c} \frac{\partial E_y}{\partial t} + q(U_y + E_y) dx$ denotes the total current in the nondimensional form. In this paper, three main regimes with $Wi = 0.05, 0.2,$ and 0.5 are considered, which correspond to weakly, moderately, and strongly elastic fluids, respectively.

A. Model verification

The electroconvection in a liquid layer is in a steady conduction state when the value of T is relatively low. As T increases, the steady conduction loses its stability and stationary convection sets in. This instability of the conduction state is called the first instability. Table I gives the maximum vertical velocity V_{\max} and electric Nusselt number of the steady-state convection corresponding to different values of M when $T = 190$, together with the results of Wu *et al.* [56]. It can be seen that there is good agreement between the two sets of results.

Periodic oscillatory convection emerges later following the first instability. Figure 2 shows the phase portraits at the fixed point A and the power spectra densities of the maximum velocity for $T = 230$ and 277 . When $T = 230$, it can be seen that the flow motion is typically periodic. The phase diagram is a closed loop. The power spectrum corresponds to a fundamental frequency $f = 0.687$ and its harmonic frequencies $2f, 3f,$ etc. The amplitude of the fundamental frequency is much larger than those of the higher harmonics. When $T = 277$, a subharmonic frequency appears, accompanied by the fundamental frequency ($f_1 = 0.719$), which indicates that the flow is quasiperiodic. With the

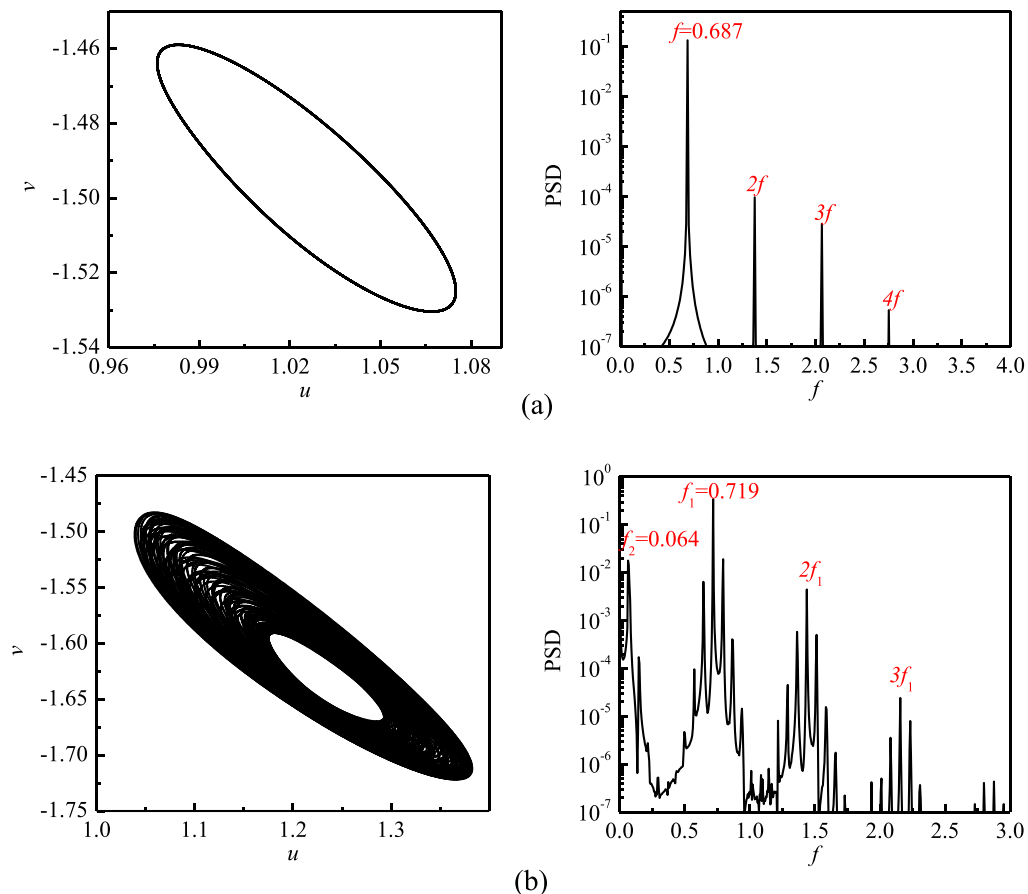


FIG. 2. Oscillating state in a Newton fluid for (a) $T = 230$ and (b) $T = 277$. The left panels are the phase portraits of (u, v) at the point A, and the right panels are plots of the PSD with a logarithmic vertical scale.

same parameters, the fundamental frequency obtained by Wang *et al.* [47] through FVM is 0.692 and 0.724 for $T = 230$ and 277, respectively. It can be seen that the present results are in good agreement with the previous reference.

In the experiments by Lacroix *et al.* [15], a scaling law $Ne \sim M^{1/2}$ was obtained when the inertial terms were dominant. To investigate this relationship numerically, a large $T = 20\,000$ is chosen so that the inertial terms are dominant in the range of M under consideration. To obtain the time-average Ne , we average Ne over long periods of time. Figure 3 shows the variation in electric Nusselt number as a function of $M^{1/2}$. It can be seen that Ne varies nearly linearly with $M^{1/2}$, which is in agreement with the experimental findings. However, it is worth noting that because the experiment is three dimensional, the slope of the linear relationship will not be the same in the two-dimensional simulation, which is easy to understand.

In addition, the codes in this paper have been verified by the hydrostatic solution of electroconvection and the lid-driven cavity flow of viscoelastic liquids. These verifications were presented in our previous paper [40], where good agreement was observed. Thus, all these results suggest that our codes can accurately simulate the problem considered in the present paper.

B. Weakly elastic fluids

The weakly elastic effect with $Wi = 0.05$ is first chosen to investigate the interplay between elasticity and fluid motion in electroconvection. By increasing T , we want to examine which of

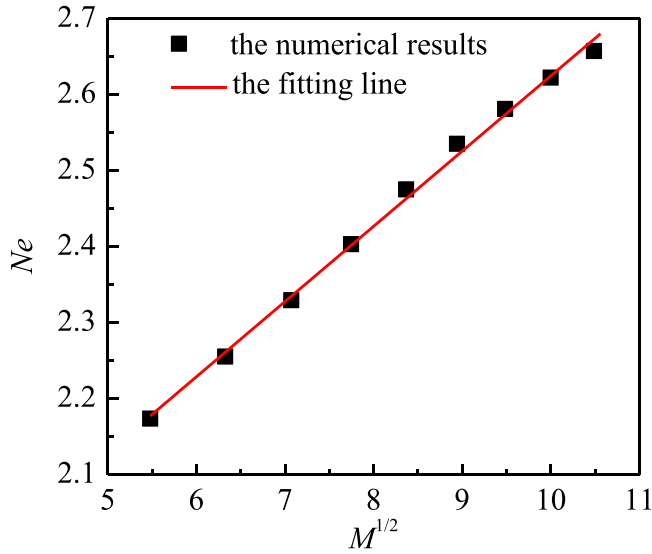


FIG. 3. Variation of the electrical Nusselt number Ne with $M^{1/2}$.

the further instability can be found. For a Newtonian fluid or a viscoelastic fluid with weak elastic effect, the flow varies from a hydrostatic state to a stable one-cell asymmetric steady state when T is slightly above the value for onset of instability. With increasing T , a Hopf bifurcation occurs, and the flow develops into oscillating motion but still with only one cell. With further increase in T , the flow turns into a two-cell symmetric steady state. Here, we choose the solution with $T = 600$ and $Wi = 0.05$ as an example, and the corresponding charge distribution and streamlines are shown in Fig. 4. For electroconvection in a Newtonian fluid, periodic oscillatory convection emerges later, after the two-cell symmetric steady state, and then a quasiperiodic route to chaos is established [11,47]. However, in a viscoelastic fluid, the evolution of the flow motion is quite different. A sequence of maximum velocity records, phase portrait, and corresponding power spectral densities as T increases for $Wi = 0.05$ are shown in Fig. 5.

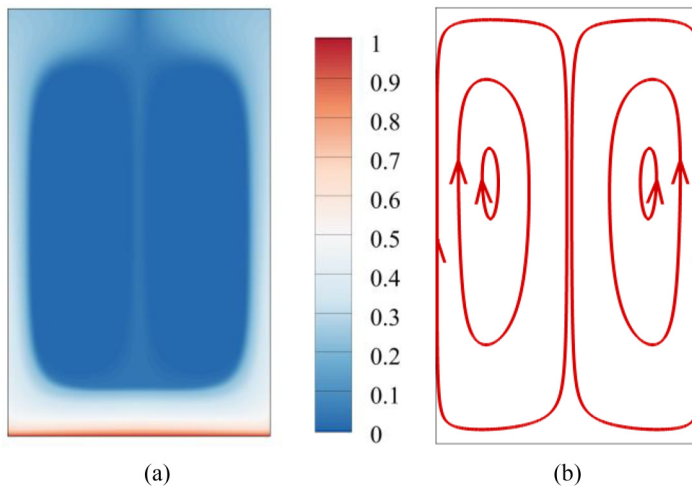


FIG. 4. Charge density isocontours (a) and streamlines (b) for $T = 600$ and $Wi = 0.05$.

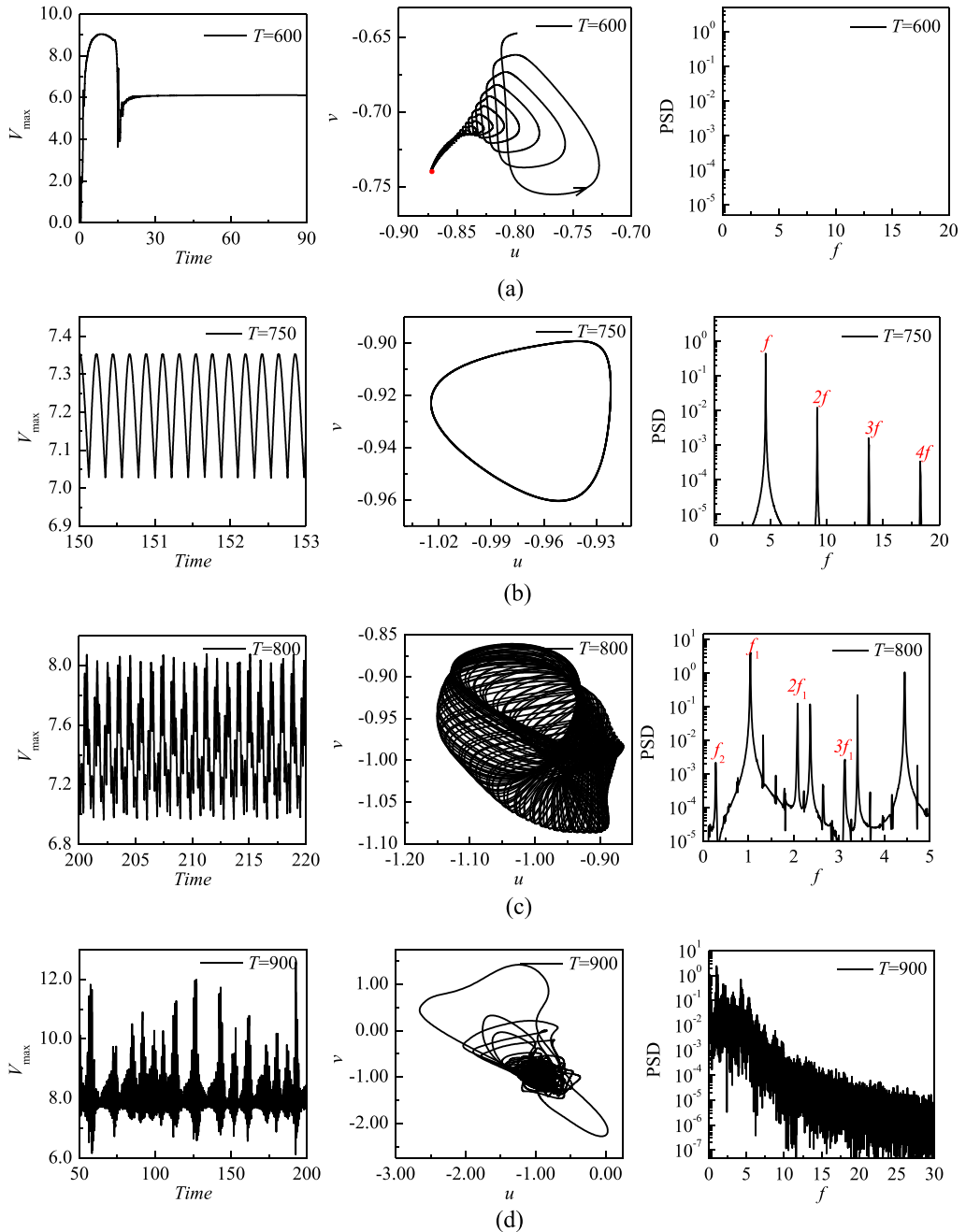


FIG. 5. Maximum velocity records (left panels), phase portraits of (u, v) at point A (middle panels), and power spectral densities (right panels) for $Wi = 0.05$ showing the sequence of instabilities from steady to nonperiodic flow: (a) $T = 600$, two-cell symmetric steady flow; (b) $T = 750$, periodic state; (c) $T = 800$, quasiperiodic state; (d) $T = 900$, nonperiodic state.

For $T = 600$, the disturbance of the flow field accumulates slowly in the initial stage [as shown in Fig. 5(a)]. When the disturbance has accumulated to a certain extent, the flow field goes through a stage of rapid development and reaches the first convection state of the one-cell structure. In this state, the flow field is potentially unstable. After a period of transition, it eventually becomes another steady state. This process can also be seen in the phase portrait, which regresses to a single limit point [red point in Fig. 5(a)]. The flow field in the final steady state is characterized by two symmetrical vortex structures and an apparently charge-free region. The onset of periodic oscillation for a two-cell structure is between $T = 480$ and 485 [57] for a Newtonian fluid. It is found that at a low Weissenberg number, the elastic effect delays the bifurcation from a two-cell steady flow to a periodic flow. This phenomenon will be discussed in detail in Sec. IV E. When the value of T is increased, the flow undergoes a Hopf bifurcation, as shown in Fig. 5(b). The sizes of the two convection cells fluctuate, which results in one larger cell and one smaller cell. The power spectrum shows a fundamental frequency with harmonics at integral multiples of the fundamental frequency. When T increases to 800, as shown in Fig. 5(c), although the velocity time series also oscillates, there is no obvious period. There is no longer a single closed-loop trajectory in the phase diagram, but instead many nonoverlapping trajectories on a torus, and two fundamental frequencies appear in the power spectrum at this time. Within the allowable range of standard error, the frequencies at all peaks can be identified as linear combinations of two basic fundamental frequencies, indicating that the flow is in a quasiperiodic state at this time. The onset of the subharmonic frequency might be explained by a secondary time-dependent instability of the oscillating flow [58]. When T increases to 900, as shown in Fig. 5(d), the velocity records become complicated and irregular. The trajectories in the phase diagram are also twisted into a ball, and the power spectrum shows obvious broadband characteristics. In the case of unsteady flow with a broadband spectrum, the power spectrum cannot be used to determine whether the system is random or deterministic, because the many fundamental frequencies of the quasiperiodic state may lead to a misleading judgment of the flow as being chaotic. To further quantify the time dependence of the flow, calculations of the fractal dimension and Lyapunov exponent are necessary.

In fact, this strange behavior of the flow can be described by calculating the fractal dimension of the related strange attractor. Therefore, we introduce a method for calculating the fractal dimension, namely, the correlation dimension [59], which is defined as

$$d_C = \lim_{r \rightarrow 0} \frac{\ln(C_p(r))}{\ln r}, \quad (26)$$

where $C_p(r)$ is the number of data pairs for which the distance between two points in phase space is less than r , divided by N^2 , and is given by

$$C_p(r) = \lim_{N \rightarrow \infty} \frac{1}{N^2} \sum_{\substack{i,j=1 \\ i \neq j}}^N h(r - |\vec{X}_i - \vec{X}_j|), \quad (27)$$

where h is the Heaviside function, \vec{X}_i and \vec{X}_j are a pair of data points in the p -dimensional phase space, and N is the total number of data points. As the phase-space dimension p increases, the slope of the linear part of the relationship between $\ln C(r)$ and $\log r$ becomes independent of p (except for white noise), and the slope is the value of the fractal dimension. For periodic flow, the slope is close to 1, for two-frequency quasiperiodic flow, it is close to 2, and for deterministic chaos, it is close to k , where k is a real number greater than 2 [60].

Another technique to further quantify the strangeness or chaos of strange attractors is calculation of Lyapunov exponents. It is generally believed that a strange attractor has at least one positive Lyapunov exponent, which represents the exponential divergence of two adjacent trajectories. Since the attractor is bounded, this exponential divergence means that a systematic folding process of fractal dimension usually occurs. Grassberger and Procaccia [61] pointed out that the lower bound

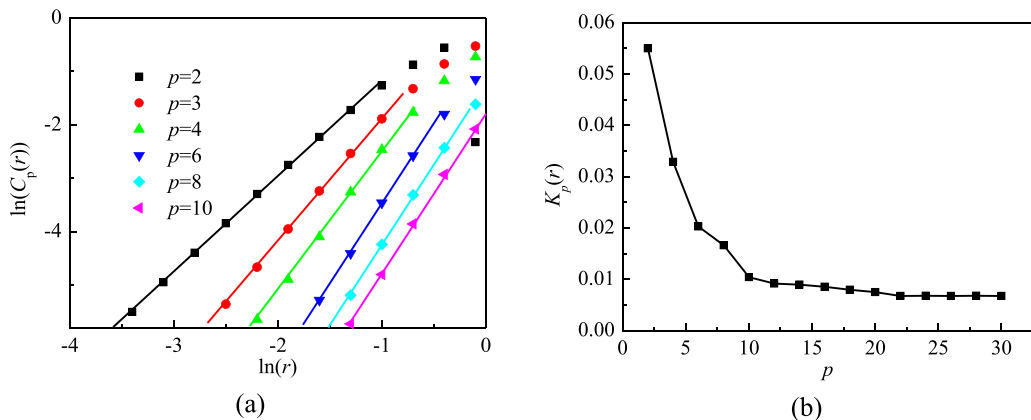


FIG. 6. Chaos judgment for $T = 900$ and $Wi = 0.05$: (a) fractal dimension computation; (b) lower bounds of the sums of positive Lyapunov exponents.

of the sum of positive Lyapunov exponents can be determined by the following formula:

$$K_2 = \lim_{\substack{p \rightarrow \infty \\ r \rightarrow 0}} \frac{1}{\tau} \ln \frac{C_p(r)}{C_{p+1}(r)} = \lim_{\substack{p \rightarrow \infty \\ r \rightarrow 0}} K_p(r). \quad (28)$$

Figure 6(a) shows the calculation of the fractal dimension when $T = 900$. It can be seen that as the phase-space dimension p increases, the slope of the linear part of the curve continues to increase until $p \geq 6$. The corresponding fractal dimension is $d_c = 3.05$ which is greater than 2. Looking at the variation of the lower bound $K_p(r)$ of the positive Lyapunov exponent as shown in Fig. 6(b), it can be seen that $K_p(r)$ remains greater than zero as p increases, indicating that at least one Lyapunov exponent is greater than zero. From the above analysis, it can be judged that the flow corresponding to $T = 900$ is indeed chaotic. However, the oscillation is quasiperiodic for the electroconvection in a Newtonian fluid under the same working conditions. Thus, it is also worth noting that the onset of chaotic behavior for a viscoelastic fluid with $Wi = 0.05$ occurs at a value of T lower than that corresponding to a Newtonian fluid. In the following study, all chaotic oscillations are determined by the fractal dimension and Lyapunov exponent.

We now examine the flow when T exceeds 900, and the results are shown in Fig. 7. Interestingly, with the increase of T from 900 to 950, the degree of chaos does not directly increase but the flow turns into a quasiperiodic oscillation again. For $T = 950$, the fundamental frequency is evident in Fig. 7(a), which is distinctly different from the broadband noise in Fig. 5(d) that typically characterizes chaotic behavior. Multiple linear combinations of f_1 and f_2 illustrate the strong nonlinearity of this process. As T is further increased to 1100, as shown in Fig. 7(b), the subharmonic frequency disappears, and the flow turns into a periodic state. Then the limit cycle loses its stability when $T = 1200$, and the flow turns into a quasiperiodic state, as shown in Fig. 7(c). At a still higher electric Rayleigh number of $T = 1300$, the spectrum becomes disordered, and chaotic fluctuations reappear [as shown in Fig. 7(d)].

When compared with the results for a Newtonian fluid, it can be seen that there is an additional periodic regime between the chaotic regime (between $T = 900$ and 1300) for electroconvection in a viscoelastic fluid with a low Weissenberg number.

C. Moderately elastic fluids

In this subsection, the value of Wi is set equal to 0.2. When T is gradually increased above the critical value for the onset of convection, the phenomenon in the initial stage is similar to that for $Wi = 0.05$, and so the results will not be described again there. However, after the two-cell symmetric

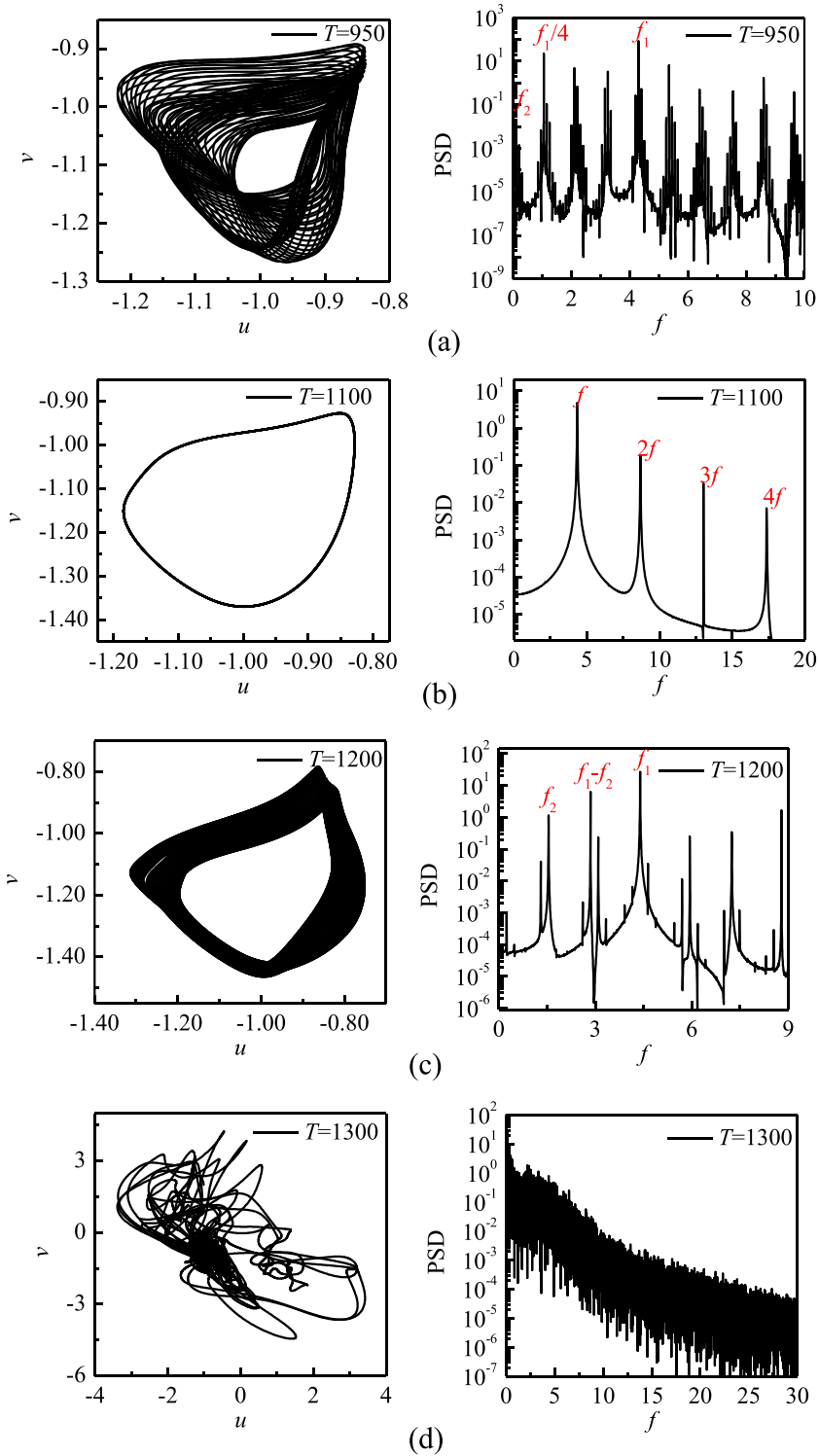


FIG. 7. Phase portraits of (u, v) at point A (left panels) and power spectra density (right panels) for $Wi = 0.05$: (a) $T = 950$, quasiperiodic state; (b) $T = 1100$, periodic state; (c) $T = 1200$, quasiperiodic state; (d) $T = 1300$, nonperiodic state.

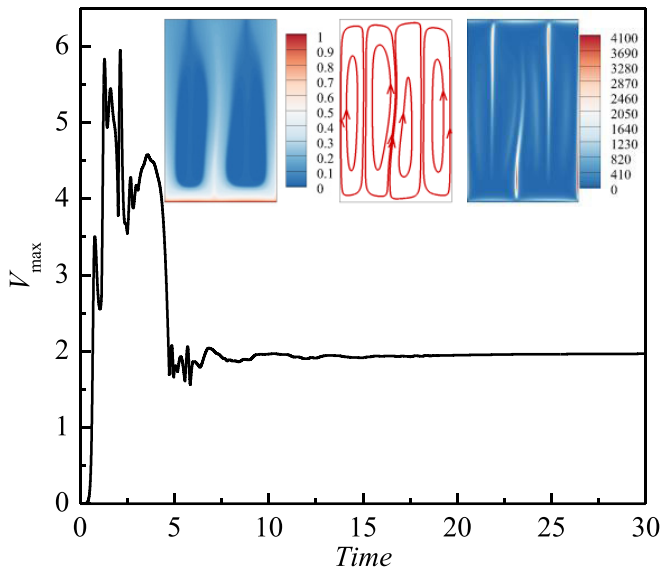


FIG. 8. Time evolution of the maximum velocity for $T = 650$ and $Wi = 0.2$. The insets show the charge density distribution, streamlines, and first principal normal stress difference in the final steady state.

state becomes unstable through a Hopf bifurcation, and with increasing T , it is interesting that the flow bifurcates into a steady structure with four cells. This phenomenon occurs when $T = 650$. The time evolution of the maximum velocity for $T = 650$ is displayed in Fig. 8 and shows that the flow finally reaches a steady convective state. In addition, a four-cell asymmetric steady flow structure can be seen from the inset.

To explain the appearance of the four-cell structure, we need to introduce the definition of the first principal normal stress difference N_p which is defined as [41]

$$N_p = \tilde{T}_1 - \tilde{T}_2, \quad (29)$$

where \tilde{T}_1 is the eigenvalue of the first principal axis of the tensor $\mathbf{T} = \frac{1}{Wi}(\mathbf{C} - \mathbf{I})$, and \tilde{T}_2 is the eigenvalue with eigenvector perpendicular to the first eigenvector. The N_p distribution corresponding to $T = 650$ is shown in the inset of Fig. 8. It can be seen that the large values of N_p are distributed between adjacent convection cells. Dubief and Terrapon [41] pointed out that N_p in plumes will push adjacent convection cells apart, thereby splitting the cell. This phenomenon leads to the fact that the horizontal length of the convection cell is shorter than that of the Newtonian flow. Therefore, a flow pattern with two cells will bifurcate into four cells for suitable values of Wi . The asymmetric steady state of a viscoelastic fluid's in a perfectly symmetric geometry has also been reported in experiments [62] and numerical simulations [63] for flow at the “cross-slot” geometry. Arratia *et al.* [62] hypothesized that stretching of polymer molecules near the hyperbolic point might cause this phenomenon. By contrast, Poole *et al.* [63] suggested that the asymmetry results from the compressive nature of the flow upstream of the stagnation point rather than the high elongational stresses in the flow downstream of the stagnation point. Similar to RBC with polymer additives [41], large N_p regions seem to be mainly confined to the extensional flow region near the stagnation point, in which the electric plume lifts off from the lower electrode plate. In the root region of the electric plume from its inception, the flow is primarily extensional. It can also be seen from the inset in Fig. 8 that the distribution of N_p deviates more from the center of the computational domain near the stagnation point, while it still seems to be close to left-right symmetry in other regions. Thus, we predict that high elongational stress in the flow downstream of the stagnation point results in the asymmetric flow pattern in this paper, similar to that in Ref. [59].

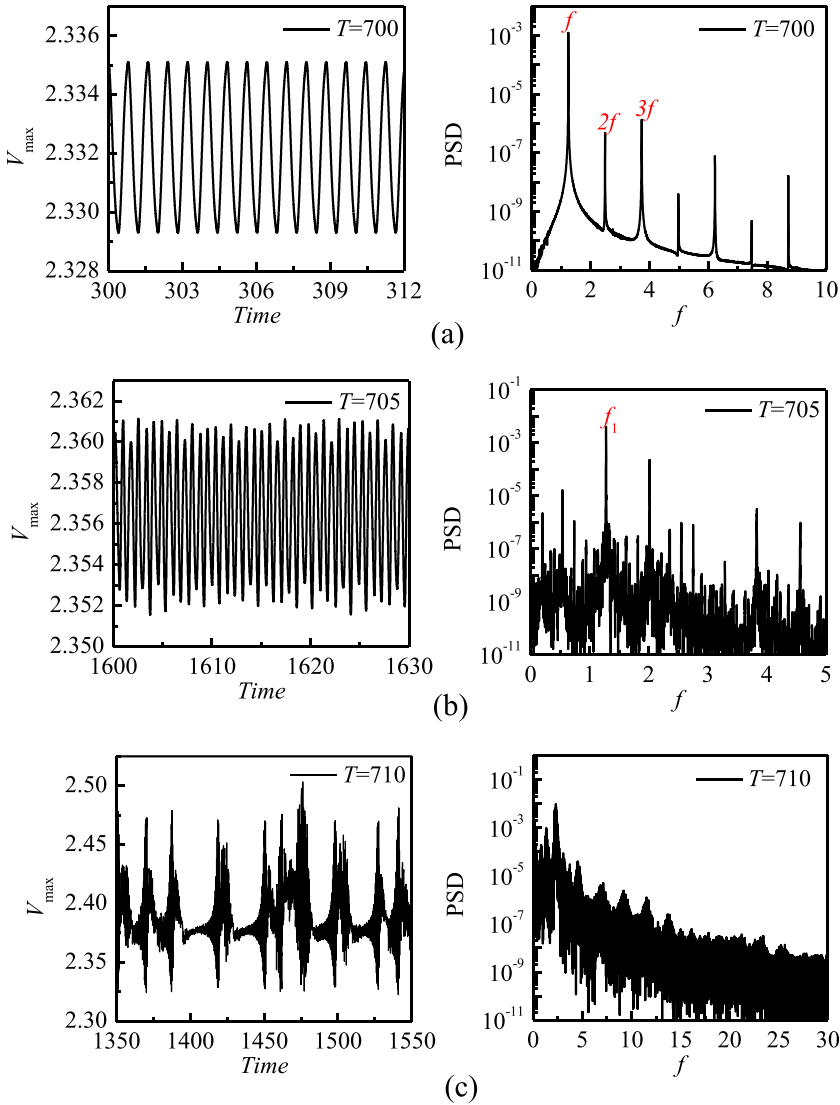


FIG. 9. Maximum velocity records (left panels) and power spectra density (right panels) for $Wi = 0.2$: (a) $T = 700$, periodic state; (b) $T = 705$, quasiperiodic state; (c) $T = 710$, nonperiodic state.

The sequence of instabilities after the asymmetric pattern is shown in Fig. 9. With an increase of T to 700, the flow with four asymmetric cells will undergo a Hopf bifurcation and evolve into an oscillatory flow. Figure 9(a) shows that the velocity oscillates periodically, although the amplitude of oscillation is tiny. With an increase of T to 705, as shown in Fig. 9(b), the oscillation amplitude increases, and the flow becomes quasi-periodic. Above this T value, as shown in Fig. 9(c), the noise grows rapidly. The spectra at $T = 710$ are almost featureless, and the underlying basic flow is hardly distinguishable, which indicate that the flow develops into chaos.

D. Strongly elastic fluids

We now examine the solutions when the Weissenberg number is equal to 0.5. After the onset of convection, the flow evolves from a one-cell steady state to a periodic oscillation state as T

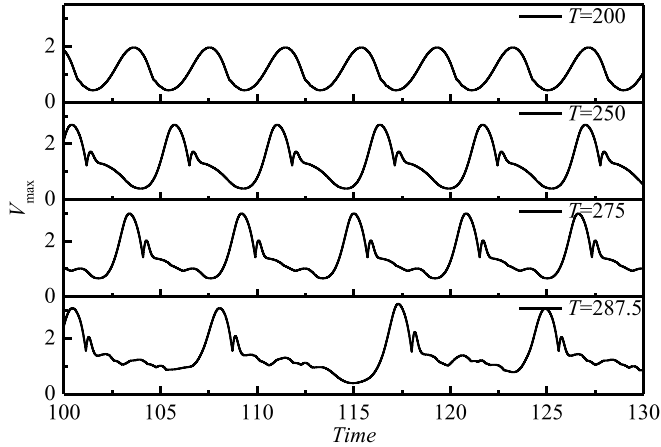


FIG. 10. Maximum velocity records for $Wi = 0.5$ at $T = 200, 250, 275,$ and 287.5 .

is gradually increased. Figure 10 shows the time evolution of the maximum velocity for different values of T . The oscillation behavior gets more and more complicated with increasing T , and there is a bifurcation from a periodic structure ($T = 200, 250,$ and 275) to a quasiperiodic one ($T = 287.5$). However, for the current Wi value, a stable two-cell structure cannot be obtained, which is quite different from the cases of weakly elastic and moderately elastic fluids.

As T is further increased, the flow bifurcates into chaos, as shown in Fig. 11 at $T = 295$. Although the power spectrum has obvious peaks, the corresponding fractal dimension is 2.62. As T is increased to $T = 305$, the oscillation evolves from chaotic to periodic. It can be seen that after an initial transient of highly erratic fluctuations, the flow converges to a periodic solution, and as T continues to increase, the early chaotic evolution process becomes shorter (e.g., at $T = 330$). Chimanski *et al.* [64] pointed out that the nonattractive chaotic set of the chaotic saddle is the cause of such chaotic transients.

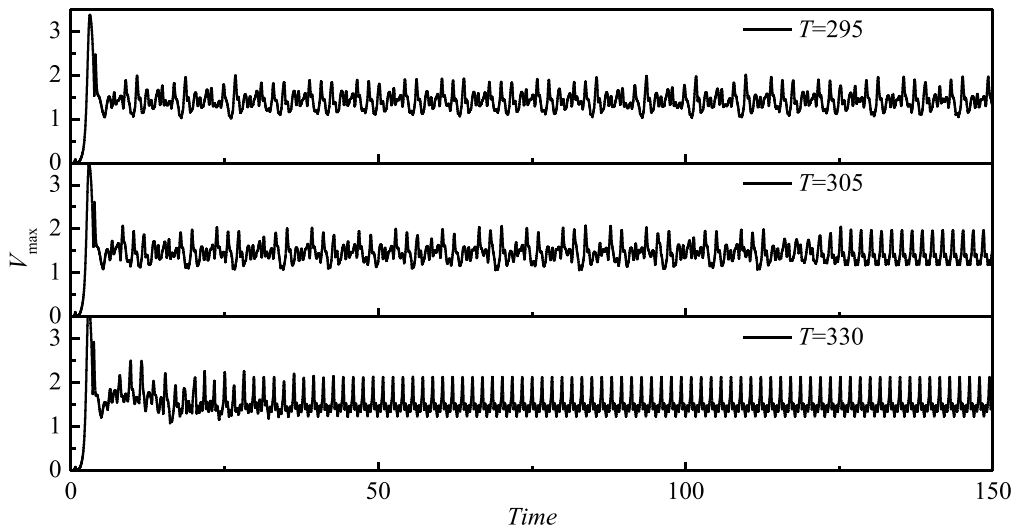


FIG. 11. Maximum velocity records for $Wi = 0.5$ at $T = 295, T = 305,$ and $T = 330$.

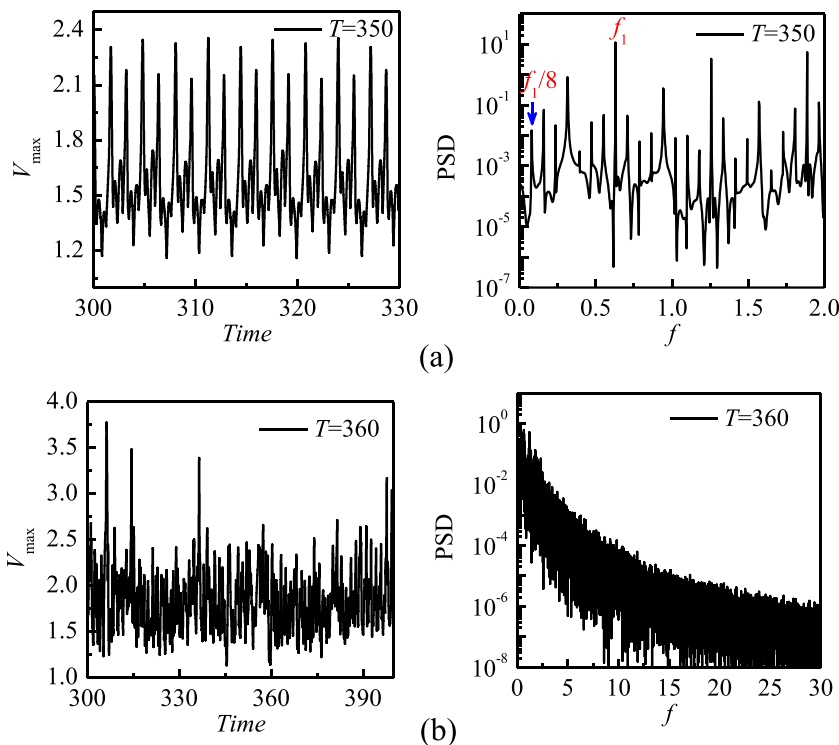
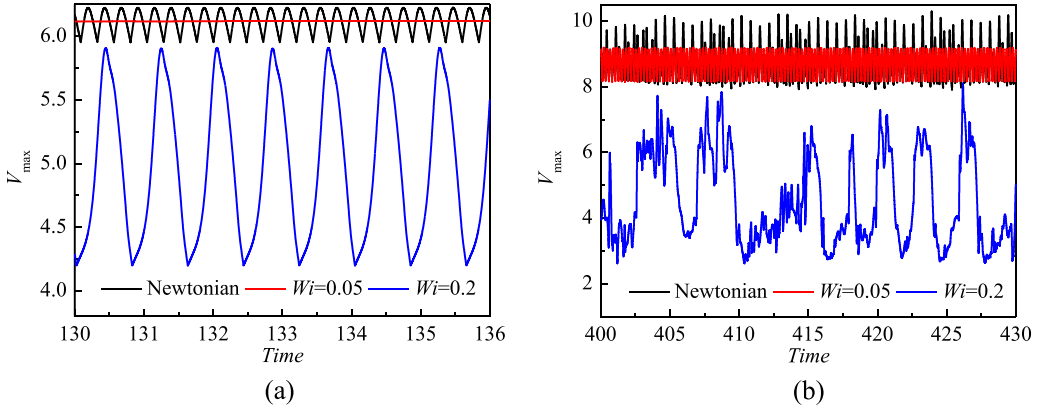


FIG. 12. Maximum velocity records (left panels) and power spectra density (right panels) for $Wi = 0.5$: (a) $T = 350$, quasiperiodic state; (b) $T = 360$, nonperiodic state.

After the periodic oscillation regime, the system bifurcates into a period-8 flow. The power spectrum near the onset of the bifurcation ($T = 350$) is shown in Fig. 12(a). Although the fluctuation in V_{\max} is quite complicated, all the peaks in the power spectrum are at $f_1/8$ and its multiples. At a still higher electric Rayleigh numbers of $T = 360$, as shown in Fig. 12(b), chaotic flow reappears.

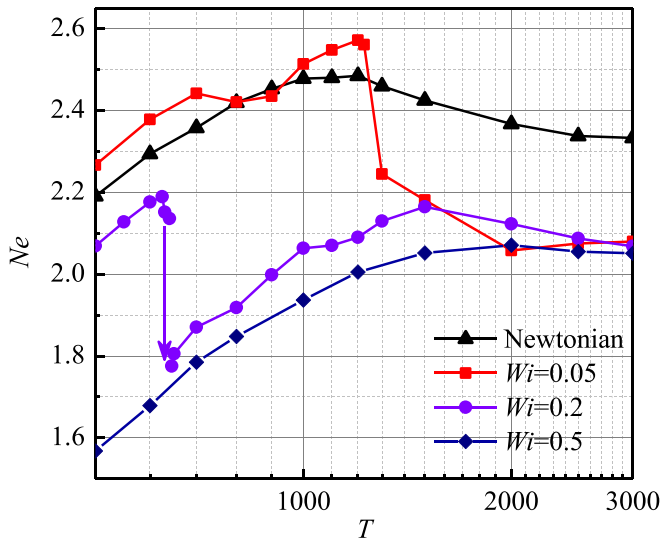
E. Comprehensive comparison

A comprehensive comparison of the above results shows that the greater the value of Wi , the earlier the system enters chaotic state. The examination of the influence of elasticity on the oscillations of the two-cell flow in this paper indicates that the onset of these oscillations may be delayed or advanced. To analyze this phenomenon, Fig. 13 provides some insight into the evolution of maximum velocity as a function of time for different Weissenberg numbers. For the case with $T = 600$, as shown in Fig. 13(a), the electroconvection of a Newtonian fluid exhibits periodic oscillation. However, the flow is steady when the fluid is replaced by a viscoelastic fluid with $Wi = 0.05$. When Wi is increased to 0.2, the flow becomes periodic again. In addition, with increasing Wi , the oscillation amplitude of the maximum velocity first decreases and then increases. For $T = 1000$, as shown in Fig. 13(b), the effect of elasticity on the fluctuation amplitude is analogous to this phenomenon. It can be inferred that weak elasticity can suppress the oscillation amplitude of electroconvection, whereas strong elasticity plays a counterproductive role. To explain this, we introduce the fluid kinetic energy, defined as $E_k = \frac{1}{2} \int_{\Omega} (u^2 + v^2) dV$. For $T = 600$, the time-averaged values of E_k for a Newtonian fluid and for viscoelastic fluids with $Wi = 0.05$ or 0.2 are 1.91, 1.88, and 1.06, respectively, while for $T = 1000$, the corresponding values of E_k are 3.25, 2.82, and 0.89, respectively. Similar to the polymer drag reduction, in which polymers apply


 FIG. 13. Influence of the viscoelastic effect on oscillation: (a) $T = 600$; (b) $T = 1000$.

a negative torque to the motion [41,65], the polymer slows down the circulation in the convection cell. Therefore, oscillation is suppressed for weakly elastic fluids. However, when the elasticity reaches a certain level, the polymer stress exhibits steep gradients in the velocity field. Even without inertia, the flow in a viscoelastic fluid can still spontaneously show a time dependence when elastic stresses overcome viscous stresses. Therefore, it is easy to understand that the elasticity amplifies the oscillation. In view of this phenomenon, by selecting an appropriate viscoelastic fluid, it should be possible to improve the stability of the system as required. Besides, the flow of electroconvection is strongly perturbed for values of the elasticity, and this may be utilized to produce mixing.

The influence of elasticity on heat transfer has been examined extensively in recent years. The electric Nusselt number characterizes the current intensity of electroconvection, somewhat similarly to the Nusselt number in thermal convection. To figure out how elasticity influences the electric current in the bulk flow of electroconvection, a series of numerical simulations are carried out, with results shown in Fig. 14. For the oscillating flows obtained in this paper, we take the average value of Ne over a long period of time. In a pure Newtonian fluid, electroconvection undergoes a


 FIG. 14. Evolution of the electric Nusselt number with T for different values of viscoelastic parameters.

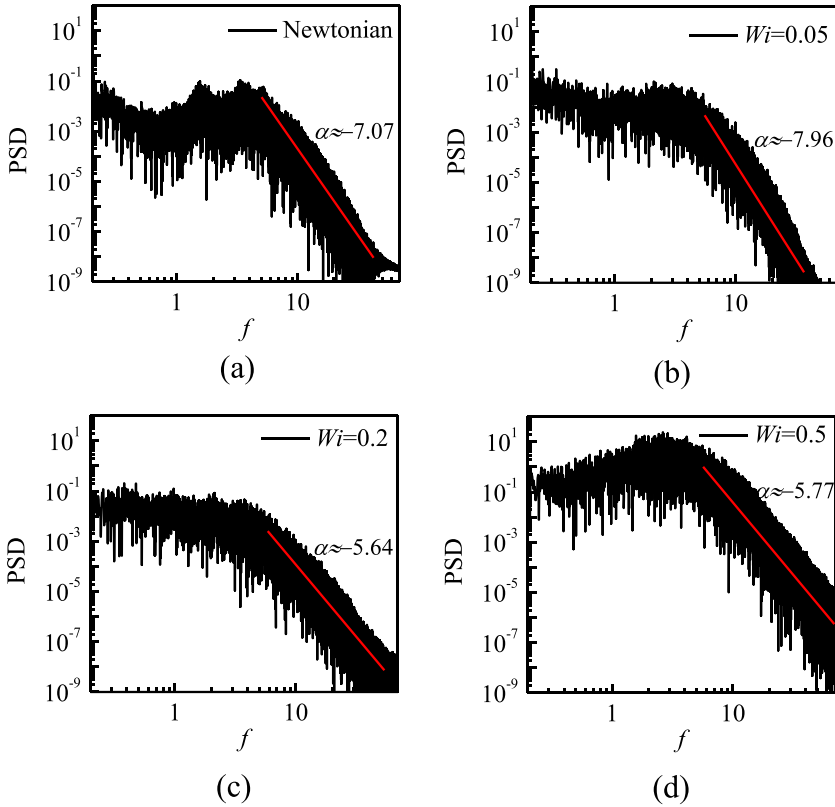


FIG. 15. Log-log plots of the power spectral density of electric Nusselt number fluctuations for $T = 1500$: (a) Newtonian fluid; (b) $Wi = 0.05$; (c) $Wi = 0.2$; (d) $Wi = 0.5$.

transition from a viscous to an inertial regime as T increases. It can be seen that Ne first increases and then decreases slightly as T increases, which is qualitatively consistent with the results of Traoré *et al.* [11] for different values of M . In the case of electroconvection in a viscoelastic fluid, elasticity plays a crucial role in addition to those of viscosity and inertia. Therefore, compared with a Newtonian fluid, the electroconvection in a viscoelastic fluid presents a more complex process, as can be observed in the curves of Ne vs T . In particular, elastic stresses tend to increase with the shear rate. Therefore, one should expect the effect of fluid elasticity to become more significant in the chaotic regime. Figure 14 highlights the vital role of the value of Wi in the electric current transfer. In a viscoelastic fluid with low Wi , the electric Nusselt number is higher than that of the corresponding Newtonian fluid when T is below 700. As T increases, the corresponding flow develops towards chaos (as shown in Fig. 5), and Ne decreases. After that, the flow changes from chaotic to periodic, and the corresponding Ne increases and again exceeds the corresponding value for a Newtonian fluid. Finally, Ne is reduced remarkably to a value lower than the corresponding value for Newtonian fluid in the process in which the flow eventually turns into chaotic. For higher Weissenberg numbers ($Wi = 0.2$ and 0.5), the results suggest that elasticity inhibits electric current transfer. For $Wi = 0.5$, the flows in the range of T values considered in Fig. 14 are all chaotic. The Coulomb force, as a convection-driven force, gradually becomes stronger with increasing T , which results in a more violent fluid motion. Computation of the fractal dimension computation shows that the degree of chaos does not increase very much in this process. Then, Ne naturally increases until saturation. However, for $Wi = 0.2$, a bifurcation from two cells to four cells is involved, which leads to a decrease in the maximum velocity of the flow. Thus, the curve of Ne vs T shows a sudden

reduction. It can be concluded that the transfer of electric current depends strongly on Wi and the flow state. Because viscoelasticity suppresses oscillation within a certain range, there is less energy loss from the system, and this contributes to enhancement of current transfer. When oscillatory vortex flows develop and become chaotic, flow resistance increases [66], and the electric Nusselt number then decreases compared with that of a Newtonian fluid. The reason is consistent with the results for the effect of the elasticity on oscillation shown in Fig. 11.

The experimental study of Malraison *et al.* [32] showed that in the inertially dominated regime, the power spectral density (PSD) of current oscillation in the high-frequency region decays with frequency, according to an asymptotic negative power law, $\text{PSD} \propto f^{-a}$, where the exponent $a = 7 \pm 1$. To investigate the effect of elasticity on a , the chaotic solutions are analyzed. The cases with $T = 1500$ are selected as being representative, and the log-log plots of the power spectral density of electric Nusselt number fluctuations for different viscoelastic parameters are shown in Fig. 15. A broad continuum range of frequencies with power-law spectral scaling behavior is visible. For the Newtonian fluid, we obtain $a = 7.07$ which is in the range found by Malraison's experiment [32]. For the viscoelastic fluid with $Wi = 0.05$, the exponent $a = 7.96$. When Wi is increased to 0.2 and 0.5, the corresponding a values are 5.64 and 5.77, respectively. Although the different exponents a found here suggest that elasticity may modify the statistical properties of the current fluctuations, the deviation from the lower bound of a value obtained in the experiment is small. We have also tested the solutions corresponding to other larger values of T and have observed similar phenomena. Within the range of Wi values considered, the viscoelasticity effect has a small effect on the range of a value. Because the value of T corresponding to the inertial regime is rather high, and the term $\frac{1-\beta}{WiT/M^2} \nabla \cdot \mathbf{C}$ on the right-hand side of the Navier-Stokes equation [Eq. (14)] is divided by T , which makes it plays a minor role compared to the Coulomb term $q\mathbf{E}$. Therefore, the values of a corresponding to different values of Wi do not deviate too much from the range of experimental results for Newtonian fluids.

V. CONCLUSIONS

In this paper, the bifurcation sequences of transitions leading to chaos of electroconvection subjected to unipolar injection in viscoelastic fluids have been investigated numerically. The influence of fluid elasticity on the flow has been examined for Weissenberg numbers in three main regimes. The chaotic behavior of oscillatory convection has been confirmed through calculations of fractal dimension and Lyapunov exponents. In addition, variations in flow pattern, oscillation amplitude, and current transfer generated by the unique oscillation behavior have been investigated.

The major conclusions to emerge from the study are that the transition sequence of electroconvection has distinctive features for different levels of elasticity. In the viscoelastic fluid, the value of the driving parameter (i.e., the electric Rayleigh number) corresponding to the onset of chaos is lower than that in the Newtonian fluid. To be more specific, the stronger the elastic effect, the earlier the chaotic behavior sets in. For both weakly elastic fluid and strongly elastic fluids, after the onset of chaos, as the electric Rayleigh number is increased further, there is a flow transition to periodic oscillatory convection and then a transition to chaos again. For a moderately elastic fluid, however, the flow undergoes a transition from two-cell oscillatory convection to a steady four-cell structure before entering chaos. Moreover, for a moderately elastic fluid, a symmetry-breaking phenomenon due to elasticity is predicted numerically for the perfectly symmetric geometry studied. We have also demonstrated that the introduction of polymers with low Weissenberg number can suppress the oscillatory fluctuations of electroconvection, whereas strong elasticity plays a counterproductive role. Moreover, elasticity may enhance the electric current transfer in a weakly elastic fluid for a certain range of driving parameters, but make this transfer poorer for most other cases. In addition, the power spectral density of the electric Nusselt number oscillation in the high-frequency region with frequency according to an asymptotic negative power law under high values of driving parameters, and the exponents of the power law for viscoelastic fluids do not deviate very much from the range of experimental results for Newtonian fluids.

In summary, the electroconvection in viscoelastic fluid exhibits a rich variety of hydrodynamic behaviors in the transition to chaos and differs greatly in this respect from that in Newtonian fluids. The research reported here can provide a reference for applications of electroconvection, such as enhancement of mixing and heat transfer. More detailed studies are ongoing, and future work includes experimental investigation of the origins of instability and expansion flows in three dimensions, where we expect there to be an even wider range of flow behaviors.

ACKNOWLEDGMENTS

This work is supported by the National Natural Science Foundation of China (Grant No. 52076055) and the Fundamental Research Funds for the Central Universities (Grant No. AUGA5710094020).

- [1] A. Castellanos, *Electrohydrodynamics* (Springer Science & Business Media, Wien, 1998).
- [2] A. I. Zhakin, *Electrohydrodynamics*, [Physics-Uspexhi](#) **55**, 465 (2012).
- [3] U. Ghosh, S. Mandal, and S. Chakraborty, Electroosmosis over charge-modulated surfaces with finite electrical double layer thicknesses: Asymptotic and numerical investigations, [Phys. Rev. Fluids](#) **2**, 064203 (2017).
- [4] T. Yamamoto and H. Velkoff, *Electrohydrodynamics in an electrostatic precipitator*, [J. Fluid Mech.](#) **108**, 1 (1981).
- [5] S. V. Fridrikh, H. Y. Jian, M. P. Brenner, and G. C. Rutledge, Controlling the Fiber Diameter During Electrospinning, [Phys. Rev. Lett.](#) **90**, 144502 (2003).
- [6] M. Jalaal, B. Khorshidi, and E. Esmaeilzadeh, Electrohydrodynamic (EHD) mixing of two miscible dielectric liquids, [Chem. Eng. J.](#) **219**, 118 (2013).
- [7] Y. Guan, X. He, Q. Wang, Z. Song, M. Zhang, and J. Wu, Monotonic instability and overstability in two-dimensional electrothermohydrodynamic flow, [Phys. Rev. Fluids](#) **6**, 013702 (2021).
- [8] Z. Lu, G. Liu, and B. Wang, Flow structure and heat transfer of electro-thermo-convection in a dielectric liquid layer, [Phys. Fluids](#) **31**, 064103 (2019).
- [9] J. Seyed-Yagoobi and J. Bryan, Enhancement of heat transfer and mass transport in single-phase and two-phase flows with electrohydrodynamics, [Adv. Heat Transfer](#) **33**, 95 (1999).
- [10] K. Luo, J. Wu, H.-L. Yi, and H.-P. Tan, Three-dimensional finite amplitude electroconvection in dielectric liquids, [Phys. Fluids](#) **30**, 023602 (2018).
- [11] P. Traoré and A. Pérez, Two-dimensional numerical analysis of electroconvection in a dielectric liquid subjected to strong unipolar injection, [Phys. Fluids](#) **24**, 037102 (2012).
- [12] P. Traoré, A. Pérez, D. Koulova, and H. Romat, Numerical modelling of finite-amplitude electro-thermo-convection in a dielectric liquid layer subjected to both unipolar injection and temperature gradient, [J. Fluid Mech.](#) **658**, 279 (2010).
- [13] R. Tobazeon, M. Haidara, and P. Atten, Ion injection and Kerr plots in liquids with blade-plane electrodes, [J. Phys. D: Appl. Phys.](#) **17**, 1293 (1984).
- [14] A. Alj, A. Denat, J. P. Gosse, B. Gosse, and I. Nakamura, Creation of charge carriers in nonpolar liquids, [IEEE Trans. Electr. Insul.](#) **EI-20**, 221 (1985).
- [15] J. Lacroix, P. Atten, and E. Hopfinger, Electro-convection in a dielectric liquid layer subjected to unipolar injection, [J. Fluid Mech.](#) **69**, 539 (1975).
- [16] P. Atten, F. McCluskey, and A. Perez, Electroconvection and its effect on heat transfer, [IEEE Trans. Electr. Insul.](#) **23**, 659 (1988).
- [17] F. McCluskey, P. Atten, and A. Perez, Heat transfer enhancement by electroconvection resulting from an injected space charge between parallel plates, [Int. J. Heat Mass Transfer](#) **34**, 2237 (1991).
- [18] P. Atten and J. Lacroix, Non-linear hydrodynamic stability of liquids subjected to unipolar injection, [J. Mécanique](#) **18**, 469 (1979).

- [19] J. Schneider and P. Watson, Electrohydrodynamic stability of space-charge-limited currents in dielectric liquids. I. Theoretical study, *Phys. Fluids* **13**, 1948 (1970).
- [20] M. Zhang, F. Martinelli, J. Wu, P. J. Schmid, and M. Quadrio, Modal and nonmodal stability analysis of electrohydrodynamic flow with and without cross-flow, *J. Fluid Mech.* **770**, 319 (2015).
- [21] M. Zhang, Weakly nonlinear stability analysis of subcritical electrohydrodynamic flow subject to strong unipolar injection, *J. Fluid Mech.* **792**, 328 (2016).
- [22] J. Wu, P. Traoré, P. A. Vázquez, and A. T. Pérez, Onset of convection in a finite two-dimensional container due to unipolar injection of ions, *Phys. Rev. E* **88**, 053018 (2013).
- [23] R. Chicón, A. Castellanos, and E. Martín, Numerical modelling of Coulomb-driven convection in insulating liquids, *J. Fluid Mech.* **344**, 43 (1997).
- [24] P. Vázquez, G. E. Georghiou, and A. Castellanos, Numerical analysis of the stability of the electrohydrodynamic (EHD) electroconvection between two plates, *J. Phys. D: Appl. Phys.* **41**, 175303 (2008).
- [25] P. Vázquez and A. Castellanos, Numerical simulation of EHD flows using discontinuous Galerkin finite element methods, *Comput. Fluids* **84**, 270 (2013).
- [26] K. Luo, J. Wu, H.-L. Yi, and H.-P. Tan, Lattice Boltzmann model for Coulomb-driven flows in dielectric liquids, *Phys. Rev. E* **93**, 023309 (2016).
- [27] K. Luo, J. Wu, H.-L. Yi, L.-H. Liu, and H.-P. Tan, Hexagonal convection patterns and their evolutionary scenarios in electroconvection induced by a strong unipolar injection, *Phys. Rev. Fluids* **3**, 053702 (2018).
- [28] M. Paul, M. Einarsson, P. Fischer, and M. Cross, Extensive chaos in Rayleigh-Bénard convection, *Phys. Rev. E* **75**, 045203(R) (2007).
- [29] R. Chertovskih, E. Chimanski, and E. Rempel, Route to hyperchaos in Rayleigh-Bénard convection, *Europhys. Lett.* **112**, 14001 (2015).
- [30] A. Kourmatzis and J. Shrimpton, Turbulent three-dimensional dielectric electrohydrodynamic convection between two plates, *J. Fluid Mech.* **696**, 228 (2012).
- [31] A. Castellanos, Coulomb-driven convection in electrohydrodynamics, *IEEE Trans. Electr. Insul.*, **26**, 1201 (1991).
- [32] B. Malraison and P. Atten, Chaotic Behavior of Instability due to Unipolar Ion Injection in a Dielectric Liquid, *Phys. Rev. Lett.* **49**, 723 (1982).
- [33] A. Castellanos, A. Pérez, and R. Chicon, Chaotic electroconvection in a layer of dielectric liquid subjected to unipolar injection: Maximal Lyapunov exponents, *Int. J. Bifurcation Chaos* **12**, 2523 (2002).
- [34] T.-F. Li, Z.-G. Su, K. Luo, and H.-L. Yi, Transition to chaos in electro-thermo-convection of a dielectric liquid in a square cavity, *Phys. Fluids* **32**, 013106 (2020).
- [35] F. Li, X.-Y. Yin, and X.-Z. Yin, Shape oscillations of a viscoelastic droplet suspended in a viscoelastic host liquid, *Phys. Rev. Fluids* **5**, 033610 (2020).
- [36] F. Li, S.-Y. Ke, X.-Y. Yin, and X.-Z. Yin, Effect of finite conductivity on the nonlinear behaviour of an electrically charged viscoelastic liquid jet, *J. Fluid Mech.* **874**, 5 (2019).
- [37] S. Berti, A. Bistagnino, G. Boffetta, A. Celani, and S. Musacchio, Two-dimensional elastic turbulence, *Phys. Rev. E* **77**, 055306(R) (2008).
- [38] S. Sid, V. E. Terrapon, and Y. Dubief, Two-dimensional dynamics of elasto-inertial turbulence and its role in polymer drag reduction, *Phys. Rev. Fluids* **3**, 011301(R) (2018).
- [39] C. Yuan, H. N. Zhang, Y. K. Li, X. B. Li, and F. C. Li, Nonlinear effects of viscoelastic fluid flows and applications in microfluidics: A review, *Proc. Inst. Mech. Eng., Part C* **234**, 4390 (2020).
- [40] Z.-G. Su, Y.-M. Zhang, K. Luo, and H.-L. Yi, Instability of electroconvection in viscoelastic fluids subjected to unipolar injection, *Phys. Fluids* **32**, 104102 (2020).
- [41] Y. Dubief and V. E. Terrapon, Heat transfer enhancement and reduction in low-Rayleigh number natural convection flow with polymer additives, *Phys. Fluids* **32**, 033103 (2020).
- [42] R. Benzi, E. Ching, and V. Chu, Heat transport by laminar boundary layer flow with polymers, *J. Fluid Mech.* **696**, 330 (2011).
- [43] P. Atten, Electrohydrodynamic instability and motion induced by injected space charge in insulating liquids, *IEEE Trans. Dielectr. Electr. Insul.* **3**, 1 (1996).

- [44] F. Habla, M. W. Tan, J. Haßberger, and O. Hinrichsen, Numerical simulation of the viscoelastic flow in a three-dimensional lid-driven cavity using the log-conformation reformulation in OpenFOAM®, *J. Non-Newtonian Fluid Mech.* **212**, 47 (2014).
- [45] A. Pérez and A. Castellanos, Role of charge diffusion in finite-amplitude electroconvection, *Phys. Rev. A* **40**, 5844 (1989).
- [46] A. Pérez, P. Vázquez, J. Wu, and P. Traoré, Electrohydrodynamic linear stability analysis of dielectric liquids subjected to unipolar injection in a rectangular enclosure with rigid sidewalls, *J. Fluid Mech.* **758**, 586 (2014).
- [47] B.-F. Wang and T. W.-H. Sheu, Numerical investigation of electrohydrodynamic instability and bifurcation in a dielectric liquid subjected to unipolar injection, *Comput. Fluids* **136**, 1 (2016).
- [48] P. Atten, and R. Moreau, Stabilité électrohydrodynamique des liquides isolants soumis à une injection unipolaire, *J. Mécanique* **11**, 471 (1972).
- [49] S. F. Davis, TVD finite difference schemes and artificial viscosity, ICASE Report No. 84-20, NASA, Langley Research Center (1984).
- [50] P. H. Gaskell and A. K. C. Lau, Curvature-compensated convective transport: SMART, A new boundedness-preserving transport algorithm, *Int. J. Numer. Methods Fluids* **8**, 617 (1988).
- [51] C. Fernandes, V. Vukčević, T. Uroić, R. Simoes, O. S. Carneiro, H. Jasak, and J. M. Nóbrega, A coupled finite volume flow solver for the solution of incompressible viscoelastic flows, *J. Non-Newtonian Fluid Mech.* **265**, 99 (2019).
- [52] R. Fattal and R. Kupferman, Constitutive laws for the matrix-logarithm of the conformation tensor, *J. Non-Newtonian Fluid Mech.* **123**, 281 (2004).
- [53] R. Fattal and R. Kupferman, Time-dependent simulation of viscoelastic flows at high Weissenberg number using the log-conformation representation, *J. Non-Newtonian Fluid Mech.* **126**, 23 (2005).
- [54] M. Alves, P. Oliveira, and F. Pinho, A convergent and universally bounded interpolation scheme for the treatment of advection, *Int. J. Numer. Methods Fluids* **41**, 47 (2003).
- [55] Y. Guan and I. Novosselov, Numerical analysis of electroconvection in cross-flow with unipolar charge injection, *Phys. Rev. Fluids* **4**, 103701 (2019).
- [56] J. Wu, P. Traoré, A. Pérez, and P. Vázquez, On two-dimensional finite amplitude electro-convection in a dielectric liquid induced by a strong unipolar injection, *J. Electrostat.* **74**, 85 (2015).
- [57] J. Wu, P. Traore, C. Louste, L. Dascalescu, F.-B. Tian, and A. T. Perez, Effect of the mobility parameter on the oscillatory electroconvection of dielectric liquids subject to strong unipolar charge injection, *IEEE Trans. Ind. Appl.* **50**, 2306 (2014).
- [58] R. Kessler, Nonlinear transition in three-dimensional convection, *J. Fluid Mech.* **174**, 357 (1987).
- [59] P. Grassberger and I. Procaccia, Characterization of strange attractors, *Phys. Rev. Lett.* **50**, 346 (1983).
- [60] Y.-S. Li, Z.-W. Chen, and J.-M. Zhan, Double-diffusive Marangoni convection in a rectangular cavity: Transition to chaos, *Int. J. Heat Mass. Tran.* **53**, 5223 (2010).
- [61] P. Grassberger and I. Procaccia, Estimation of the Kolmogorov entropy from a chaotic signal, *Phys. Rev. A* **28**, 2591 (1983).
- [62] P. E. Arratia, C. Thomas, J. Diorio, and J. P. Gollub, Elastic Instabilities of Polymer Solutions in Cross-Channel Flow, *Phys. Rev. Lett.* **96**, 144502 (2006).
- [63] R. Poole, M. Alves, and P. J. Oliveira, Purely Elastic Flow Asymmetries, *Phys. Rev. Lett.* **99**, 164503 (2007).
- [64] E. V. Chimanski, E. L. Rempel, and R. Chertovskih, On-off intermittency and spatiotemporal chaos in three-dimensional Rayleigh-Bénard convection, *Adv. Space Res.* **57**, 1440 (2016).
- [65] K. Kim, R. J. Adrian, S. Balachandar, and R. Sureshkumar, Dynamics of Hairpin Vortices and Polymer-Induced Turbulent Drag Reduction, *Phys. Rev. Lett.* **100**, 134504 (2008).
- [66] A. Groisman and V. Steinberg, Elastic turbulence in a polymer solution flow, *Nature (London)* **405**, 53 (2000).